SCIENCE CHINA
Technological Sciences

Special Topic: Double Carbon Target: Functional Materials and their Applications
•Article•

October 2022 Vol.65 No.10: 2317–2324
https://doi.org/10.1007/s11431-021-2053-1

# Oxygen-vacancy-rich $TiO_2$ enables highly active and durable water electrolysis of urchin-like $RuO_2$ catalyst

GAO HongMei[1,2†], XIAO MeiLing[1,2†], LI GuoQiang[1,2], GAO LiQin[1,2], MENG QingLei[1,2], LUO ZhaoYan[1,2], LUO ErGui[1,2], LIU ChangPeng[1,2], JIN Zhao[1,2*], GE JunJie[1,2*] & XING Wei[1,2*]

[1] *State Key Laboratory of Electroanalytical Chemistry, Changchun Institute of Applied Chemistry, Chinese Academy of Sciences, Changchun 130022, China;*
[2] *Laboratory of Advanced Power Sources, Jilin Province Key Laboratory of Low Carbon Chemical Power Sources, Changchun Institute of Applied Chemistry, Chinese Academy of Sciences, Changchun 130022, China.*

Received December 29, 2021; accepted April 11, 2022; published online June 23, 2022

The material innovation is prerequisite to accelerating sluggish oxygen evolution reaction (OER) kinetics, thus promoting the realization of hydrogen energy community. Herein, we develop an oxygen-vacancy-rich $TiO_2$ supported $RuO_2$ catalyst ($RuO_2$@r-$TiO_2$) towards improved OER activity and stability. The oxygen vacancy on $TiO_2$ not only supplies electrons to produce lower valence Ru, but also provides sufficient anchoring site for the deposition of $RuO_2$ nanocrystal. Beyond that, it can generate strong electronic interaction between $TiO_2$ and supported $RuO_2$, and thereby tailors the intermediates' adsorption energy on the $RuO_2$ surface. As a result, the derived $RuO_2$@r-$TiO_2$ catalyst exhibits superior OER activity and stability with the overpotential of 211 mV at a current density of 10 mA $cm^{-2}$ and negligible activity degradation after 6 h operation, outperforming the non-oxygen-vacancy counterpart (223.3 mV, 12.75% activity loss) and $RuO_2$ catalyst (234.6 mV, 42.86% activity loss).

**oxygen evolution reaction, oxygen vacancy, electronic interaction, stability**

**Citation:** Gao H M, Xiao M L, Li G Q, et al. Oxygen-vacancy-rich $TiO_2$ enables highly active and durable water electrolysis of urchin-like $RuO_2$ catalyst. Sci China Tech Sci, 2022, 65: 2317–2324, https://doi.org/10.1007/s11431-021-2053-1

## 1 Introduction

Being a prospective and highly desirable energy storage option, the electricity driven water splitting technique ($H_2O \rightarrow H_2 + 1/2O_2$) based on proton exchange membrane is largely limited by the oxygen evolution reaction (OER) due to its sluggish kinetics. This multi-step process, featured with O–H* bond cleavage, O–O bond formation, the electron coupling, and the adsorption/desorption, imposes a considerable overpotential requirement even when using $IrO_2$ and $RuO_2$ based noble metal catalysts [1]. This is especially true for the ruthenium oxide materials, which lie on the apex of the parabola of the volcano curve and possess the highest OER activity due to its appropriate adsorption free energies to the oxygen related intermediates [2,3]. However, the poor stability of $RuO_2$ originated from soluble high valence Ru generated at high working voltage strongly hinders its further application. Therefore, most of the studies on $RuO_2$ electrocatalyst recently not only focus on improving its intrinsic activity, but most important also aim at enhancing its stability.

Employing carrier to support $RuO_2$ is an effective strategy because the electronic coupling between the carrier and supported $RuO_2$ could prevent Ru from deep oxidation, endowing its excellent stability. Suffering from critical working

†These authors contributed equally to this work.
*Corresponding authors (email: zjin@ciac.ac.cn; gejj@ciac.ac.cn; xingwei@ciac.ac.cn)

condition, like acidic environment and high overpotential, the proper carrier strongly demands high chemical and electrochemical stability. Although carbon is used as carrier in some reports due to its high conductivity and surface area, as well as easy preparation *in situ* derived from various organic precursors, one serious drawback of being corrosion in high working voltage prohibits its extensive application. Some metallic oxides, which are chemical and electrochemical stable, further gain more and more attention. However, it is interesting that most reports involved these stable metallic oxide supports, such as $TiO_2$, $NbO_2$ as well as $MnO_2$, were about improving the activity of $IrO_2$. The studies on enhancing stability of $RuO_2$ employing these stable metallic oxide supports are rare.

Recently, Vignolo-González et al. [4] reported a novel $RuO_2$@$TiO_2$ photocatalyst with excellent catalytic capability towards photocatalytic OER, which implies that interactions including epitaxial growth of lattice and electron transfer between $RuO_2$ and $TiO_2$ indeed exist. Inspired by this report, we speculate that well designed $RuO_2$ encapsulated $TiO_2$ system could have huge potential ability towards electrocatalytic OER due to the interaction mentioned above as well as high conductivity. Therefore, in this work, a rational designed $RuO_2$/r(a)-$TiO_2$ (rutile titanium dioxide and anatase titanium dioxide) electrocatalyst was prepared, whose physical and electrochemical properties, as well as the influence of the structure and the electronic properties of the catalyst on the OER activity and durability were also carefully characterized and investigated.

## 2 Experimental section

(1) Preparation of titanium dioxide carrier. Anatase titanium dioxide (99.9%, Aladdin, named a-$TiO_2$) was calcined in $H_2$/Ar mixed gas (JuYang, Changchun, 10%) at 1000°C for 5 h given the more stable rutile titanium dioxide with oxygen vacancy, which was denoted as r-$TiO_2$ [5–7].

(2) Preparation of electrocatalysts. $RuO_2$/r-$TiO_2$ was fabricated with a molar ratio of $n(RuO_2)$:$n(TiO_2)$ = 1:1 via wet chemical method (Scheme 1). Synthesis detail is illustrated as follows. First step, the precursor of 0.2 mmol $RuCl_3$ was infused into 4 mmol $NaBH_4$ aqueous solution containing 0.2 mmol r-$TiO_2$ under stirring. The resulted hybrid was washed with the mixture of ethanol and deionized water, and then dried in a constant temperature drying oven at 50°C for 6 h. Second step, the hybrid was then calcined in air ambience at 400°C for 1 h to obtain the urchin-like structure products, noted as $RuO_2$@r-$TiO_2$.

(3) Materials characterization. The crystal structure type and the related features of catalysts were investigated by X-ray diffraction (XRD) using a Cu Kα ($\lambda$ = 1.5405 Å) radiation source (Philips Co.) [8]. Scanning electron microscopy (SEM) measurement was taken on an XL 30 ESEM FEG field emission SEM [9]. The morphology and element distribution of catalysts were viewed by transmission electron microscopy (TEM), high resolution transmission electron microscopy (HRTEM), high-annular dark-field scanning transmission electron microscopy (STEM), and element mapping analysis with a Philips TECNAI G2 electron microscope operating at 200 kV [10]. The elementary composition and binding energy were discriminated by X-ray photoelectron spectroscopy (XPS) on a Kratos XSAM-800 spectrometer with a Mg Kα radiation source [11].

Besides the mentioned tests, some more intuitive data also certificate the character of a catalyst. Electrochemical details were evaluated by a standard three-electrode test system with an EG&G mode 273 potentiostat/galvanostat [12]. The electrolyte is 0.5 M $H_2SO_4$, the working electrode, counter electrode, and the reference electrode are $\Phi_4$ glassy carbon electrode (4 mm diameter), Pt foil, and saturated calomel electrode (SCE), respectively. The ink applied to the working electrode was prepared as follows. 3 mg of the catalyst was first dispersed in 315 μL of ethanol/Nafion (5 wt%, Aldrich Chemical Company) solution (20:1), and ultrasonic for 30 min to ensure uniform dispersion [13]. Then 5 μL of the above ink was dropped on the clean glassy carbon electrode (4 mm diameter) and dried naturally for about 10 min, with the loading 0.237 mg $cm^{-2}$ on the working electrode.

(4) Electrochemical measurements. Electrochemical characterization was performed in $N_2$-saturated 0.5 M $H_2SO_4$ solution. Five cycles of the cyclic voltammetry (CV) from a voltage range of 0.3 to 1.5 V (vs. RHE) were recorded with a sweep rate of 50 mV $s^{-1}$. Electrochemical activity of the

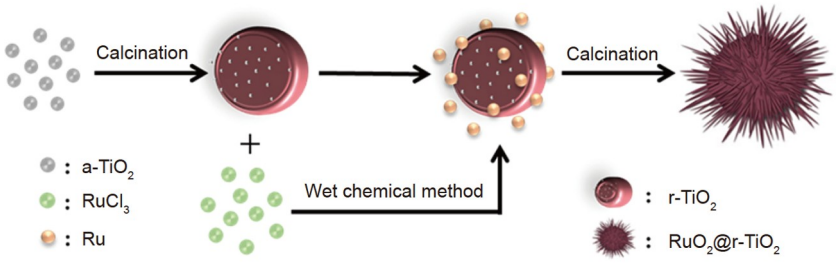


**Scheme 1** (Color online) Schematic presentation of the synthesis of the $RuO_2$@r-$TiO_2$ catalyst.

catalyst on the electrode was subjected to linear sweep voltammetry (LSV, including area activity and mass activity) from a voltage range of 1.1 to 1.7 V (vs. RHE) with a sweep rate of 5 mV $s^{-1}$ [13]. The electrochemically active surface area (ECSA) was measured by CV from double layer in a potential range of 0.867–0.967 V vs. RHE with scan rate from 10 to 50 mV $s^{-1}$. Nyquist plots of electrochemical impedance spectroscopy (EIS) reveal three components including solution resistance, charge-transfer resistance, and double-layer capacitance well fitted the semicircles [14,15]. The measurement was collected in the frequency range of 10 mHz–1000 kHz at 1.5 V vs. RHE [16]. The turnover frequency (TOF) was calculated as TOF = $(j\times A)/(4\times F\times n)$ [17–19], where $j$ (mA $cm^{-2}$) refers to the current density at a specific overpotential, $A$ refers to the area of the working electrode, $F$ refers to the Faraday constant (96500 C $mol^{-1}$), and $n$ refers to the number of moles of the materials [19]. It is hard to calculate the precise TOF value because not all elements can act as active sites for the electrocatalysts [19]. Chronopotentiometry test, which was conducted on 1 cm × 2 cm glassy carbon electrode with electrocatalyst loading of 0.237 mg $cm^{-2}$, was performed at a current density of 10 mA $cm^{-2}$ for 6 h to assess the stability of the prepared electrocatalysts [20].

## 3 Results and discussion

The a-$TiO_2$ and resulted r-$TiO_2$ were first characterized by XRD, as shown in Figure 1(a). It shows obvious diffraction peaks at 2$\theta$ values of 25.3°, 37.8°, 48°, 53.9°, 55°, and 62.7° correspond to the (101), (004), (200), (105), (211), and (204) plans of a-$TiO_2$, respectively, which means that a-$TiO_2$ is in *I*41/*amd* (141) space group (PDF card 21-1272, JCPDS). However, the sharp peaks at 27.4°, 36.1°, 41.2°, 54.3°, 56.6, and 69° can be attributed to the (110), (101), (111), (211), (220), and (301) planes of r-$TiO_2$ respectively [5,21], confirming that high temperature treatment induced the crystalline phase transition of yielded r-$TiO_2$ to *P*42/*mnm* (136) (PDF card 21-1276, JCPDS).

The given XPS spectra (Figure 1(b)) are used to confirm the electronic structure of O 1s in a-$TiO_2$ and r-$TiO_2$. The binding energy of the O 1s peak of r-$TiO_2$, which located at 527.5 eV is negatively shifted by 2.1 eV in comparison with a-$TiO_2$ (529.6 eV), implying formation of the oxygen vacancy during annealing under reducing atmosphere [22].

The XRD pattern (Figure 2(a)) of the electrocatalysts shows the crystal structure of the $RuO_2$ both in $RuO_2$@r-$TiO_2$ and $RuO_2$@a-$TiO_2$ is the same as that of homemade $RuO_2$ catalyst [PDF card 43-1027, JCPDS, space group: *P*42/*mnm* (136)]. The SEM image of $RuO_2$/r-$TiO_2$ (Figure 2(b) and (c)) shows an urchin-like structure with the surrounded needle crystal of 2 to 4 nm diameter and 10 to 70 nm length. The 0.318 nm inner-planar space suggests that this needle-like structure is corresponding to the (111) plane of $RuO_2$, which is also confirmed by the corresponding elemental colors mapping (Figure 2(f) and (g)). While the SEM and TEM images confirm that the $RuO_2$@a-$TiO_2$ often comes in small grains-like $RuO_2$ uniformly dispersed on the surface of a-$TiO_2$, as shown in Figure S1(a)–(f), which reveals that the crystalline phase of the support does not have any effect on the structure, but only the morphology of the supported $RuO_2$ nanocrystal. Notably, a small XRD peak at 44° and the binding energy at 462.2 eV in Ru $3p_{3/2}$ of $RuO_2$@r-$TiO_2$ reveal the existence of metallic Ru. According to the previous report [23], that is probably because electrons transfer from electron-enriched $TiO_2$ to supported Ru nanoparticles (which generated by reducing $RuCl_3$ in the first step of preparation of electrocatalyst) and help stabilize partial Ru cluster remaining its metallic state during heat treatment.

The electronic structure of catalysts is explored by XPS spectra. From Ru 3p and Ti 2p XPS spectra shown in Figure 3(a) we found that the binding energies at 462.2 and 464.3 eV detected in the Ru $3p_{3/2}$ are corresponding to metallic Ru (0) and Ru (IV), respectively. The peak area percentage of Ru (0) species in the $RuO_2$@r-$TiO_2$ (44.3%) is

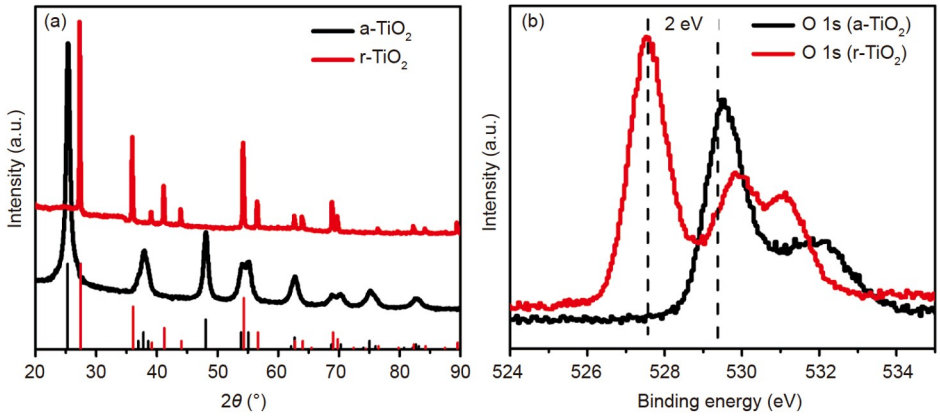


**Figure 1** (Color online) (a) XRD patterns and (b) O 1s XPS spectra of the a-$TiO_2$ and r-$TiO_2$ carriers.

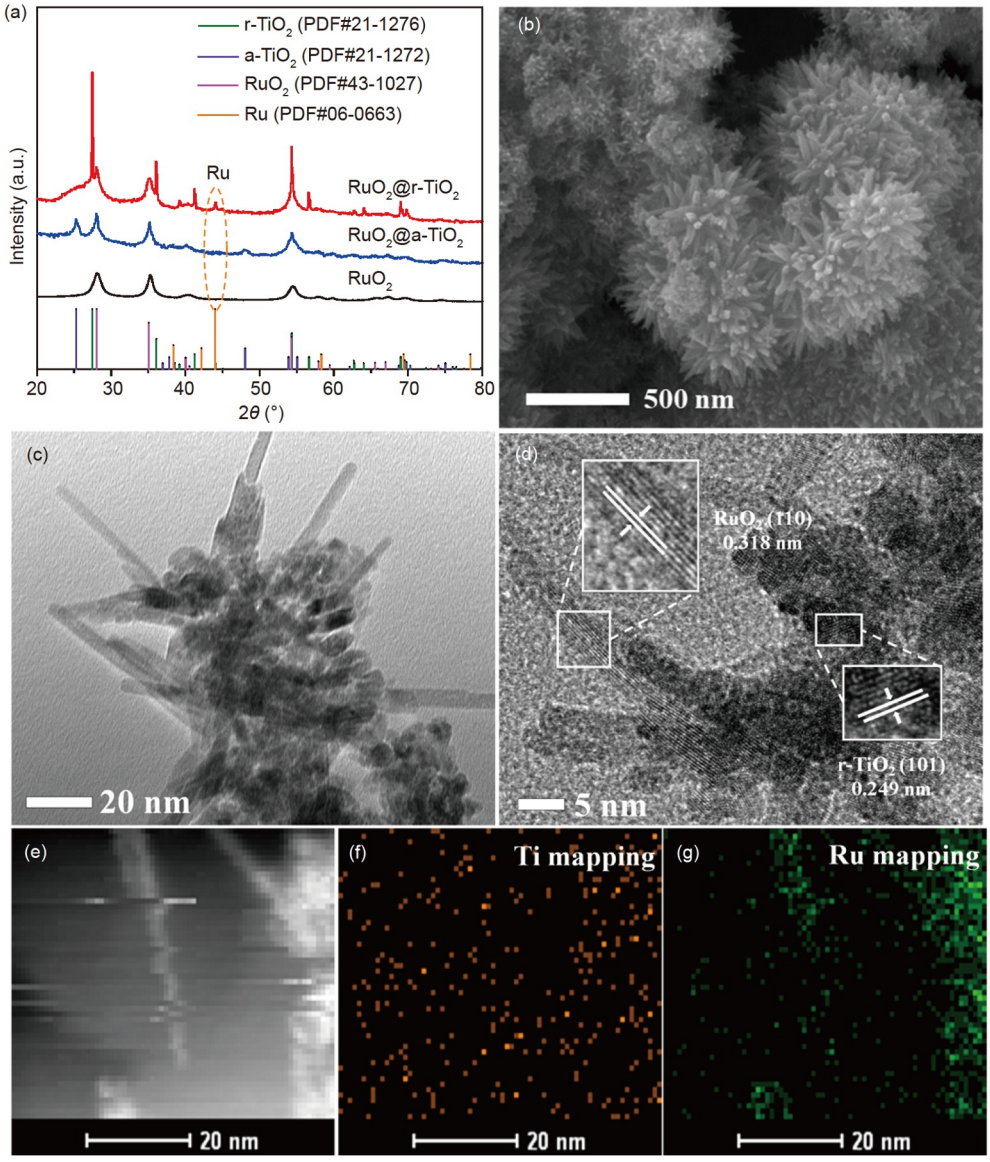


**Figure 2** (Color online) (a) XRD patterns of $RuO_2$, $RuO_2$@a-$TiO_2$, and $RuO_2$@r-$TiO_2$; (b) SEM, (c) TEM, (d) HR-TEM, (e) STEM, (f) Ti mapping and (g) Ru mapping images of $RuO_2$@r-$TiO_2$ catalyst.

higher than $RuO_2$ (39.6%) and $RuO_2$@a-$TiO_2$ (41.4%) because of the presence of oxygen vacancies, which is consistent with Figure 2(a). Meanwhile, there is an extra peak that coincides with Ru $3p_{3/2}$, which is the Ti 2p peak at 459 and 464.7 eV corresponded to Ti $2p_{3/2}$ and Ti $2p_{1/2}$ [24]. As shown in Figure 3(b), the O 1s spectra can be divided into three peaks with binding energies located at around 529.5, 531, and 532.4 eV that correspond to the lattice oxygen (O1), hydroxyl group (O2), and water molecules and/or carbon-oxygen bond (O3) [25,26]. The ratio of O2/(O1+O2+O3) in $RuO_2$, $RuO_2$@a-$TiO_2$, and $RuO_2$@r-$TiO_2$ are 21.1%, 30.7%, and 35.3% (Table S3), respectively. While in $RuO_2$@r-$TiO_2$, O2 content is higher than that of other catalysts. The XPS spectra of oxygen species in metal oxides reflect their interaction with metal cations.

According to the results above, the formation process of $RuO_2$@r-$TiO_2$ and $RuO_2$@a-$TiO_2$ could be imaged as follows. On the one hand, partial Ru located on the interface between Ru nanoparticle and r-$TiO_2$ was confined within the defects of $TiO_2$ lattice with O-vacancy and remained its metallic state. On the other hand, outside Ru was oxidized by air yielded $RuO_2$, and the matching lattice constants of $RuO_2$ and $TiO_2$ allowed the $RuO_2$ to grow along the lattice plane on the surface of r-$TiO_2$ firstly, until blocked by the defect. Then, the $RuO_2$ grew along the direction perpendicular to the r-$TiO_2$ surface given the final sea urchin-like structure. Therefore, the structure of $RuO_2$@r-$TiO_2$ exactly is r-$TiO_2$ supported needle-like $RuO_2$ encapsulating metallic Ru ($RuO_2$@Ru/r-$TiO_2$). For clarity, we keep using $RuO_2$@r-$TiO_2$ below. While for $RuO_2$@a-$TiO_2$, mismatching lattice

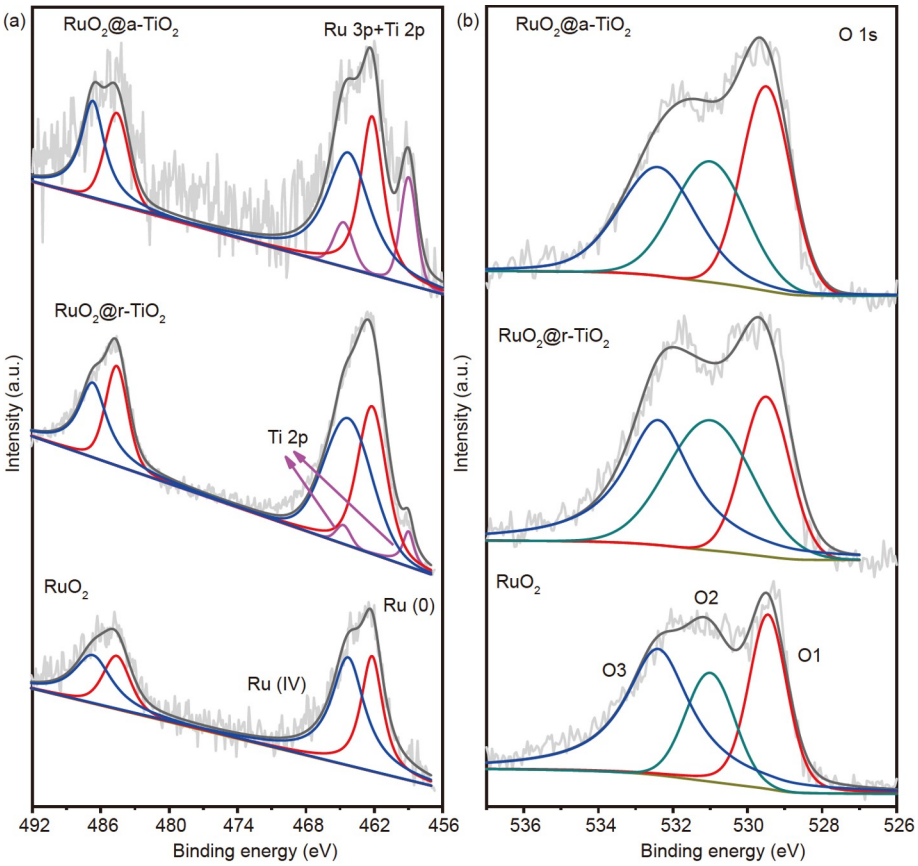


**Figure 3** (Color online) (a) Ru 3p and Ti 2p, and (b) O 1s XPS spectra regions of the $RuO_2$, $RuO_2$@a-$TiO_2$, and $RuO_2$@r-$TiO_2$ catalysts.

constants and the less defective surface of a-$TiO_2$ supply no space for extended growth of $RuO_2$, leading to the generation of its small nanoparticle structure, which then uniformly disperses on a-$TiO_2$ surface.

The OER performance of the three catalysts is estimated with an array of electrochemical tests in acidic electrolyte. In Figure S2, the carriers of a-$TiO_2$ and r-$TiO_2$ have poor OER activity from LSV test under the same condition, noting that the intrinsic activity of the prepared catalysts is attributed to the active substance of $RuO_2$ in coupled with Figure 3(a) [27,28].

As shown in Figure 4(a), $RuO_2$@r-$TiO_2$ provided quite a rapid speed of water oxidation, and it shows 211 mV overpotential (Table S2) at the current density of 10 mA $cm^{-2}$, which apparently suggests that the excellent property over the other electrocatalysts aims at less overpotential and greater current density. Otherwise, the $RuO_2$@r-$TiO_2$ catalyst property is superior to commercial $RuO_2$ (289 mV) greatly [29]. $RuO_2$@r-$TiO_2$ generates a mass specific activity of 239 mA $mg^{-1}$ (Table S2), which is 2.23 times larger than that of $RuO_2$ (107 mA $mg^{-1}$) (Figure 4(b)). As shown in Figure 4(c), $RuO_2$@r-$TiO_2$ has minimum Tafel slope as low as 47.53 mV $dec^{-1}$ in contrast to $RuO_2$ (54.49 mV $dec^{-1}$) and $RuO_2$@a-$TiO_2$ (49.97 mV $dec^{-1}$), proving the $RuO_2$@r-$TiO_2$ catalyst has faster kinetic reaction than $RuO_2$ catalysts [30,31]. The excellent oxygen revolution of $RuO_2$@r-$TiO_2$ is attributed to the sea urchin structure with large specific area. The large double-layer capacitance ($C_{dl}$) reflected the ECSA (Figure S3), which showed intrinsic OER activity of the electrocatalysts. As shown in Figure 4(d), $RuO_2$@r-$TiO_2$ has a larger $C_{dl}$ than $RuO_2$/a-$TiO_2$ and $RuO_2$, indicating that the higher ECSA comes from the 3D morphology. And $RuO_2$@r-$TiO_2$ exhibits the smallest semicircle radius (Figure 4(e)) than $RuO_2$@a-$TiO_2$ and $RuO_2$, indicating a smaller charge resistance and faster OER kinetics [32,33].

In this regard, the intrinsic activity of the optimal $RuO_2$@r-$TiO_2$ catalyst is evaluated by calculating TOF, which supplies the high TOF value of 0.132 $s^{-1}$ (Table S2) at the overpotential of 300 mV [34,35]. The prepared $RuO_2$@r-$TiO_2$ catalyst possesses the best OER performance with a higher OER activity, lower Tafel slope, and a better TOF value, which exceeds the majority Ru-based electrocatalysts in acidic solution reported in refs. [14,16,36–58] (Figure 4(g), Table S4).

The stability of the electrocatalysts was examined by chronopotentiometry technique at the current density of 10 mA $cm^{-2}$ for 6 h as revealed in Figure 4(f), and the sequence of stability is $RuO_2$@r-$TiO_2$ > $RuO_2$@a-$TiO_2$ >

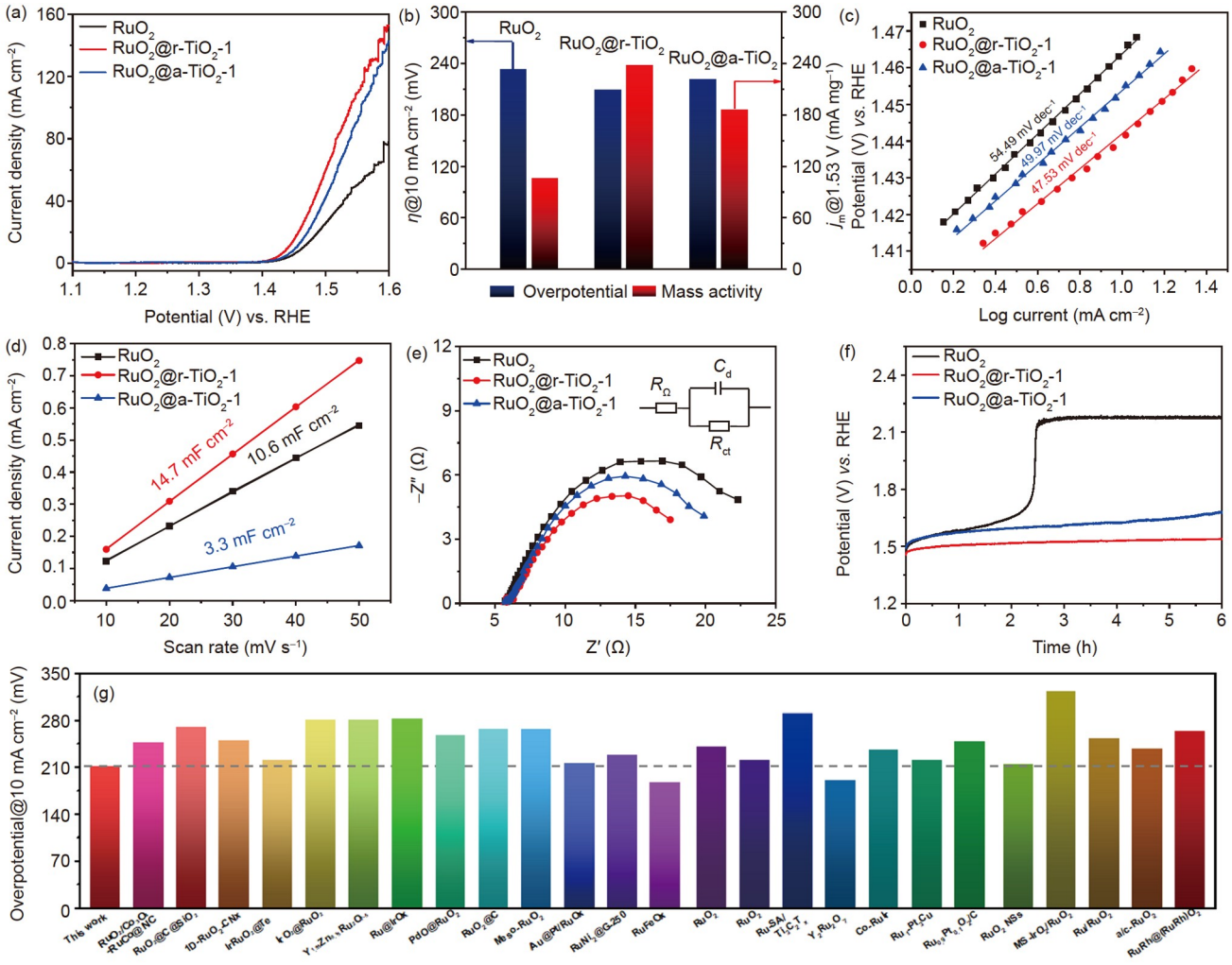


**Figure 4** (Color online) (a) LSV curves at a scan rate of 5 mV $s^{-1}$ in $N_2$-saturated 0.5 M $H_2SO_4$; (b) comparision of overpotential ($\eta$) at a current density of 10 mA $cm^{-2}$ and ruthenium dioxide mass activity ($j_m$) at 1.53 V (vs. RHE); (c) Tafel slope, (d) ECSA, (e) EIS, and (f) chronopotentiometric curves at a constant current density of 10 mA $cm^{-2}$ of $RuO_2$, $RuO_2$@r-$TiO_2$, and $RuO_2$@a-$TiO_2$ catalysts; (g) comparison of $\eta$(@10 mA $cm^{-2}$) of $RuO_2$@r-$TiO_2$ and rencently reported Ru-based catalysts at 10 mA $cm^{-2}$ in acidic media.

$RuO_2$. Different from $RuO_2$@r-$TiO_2$, $RuO_2$ catalyst is unstable in the same condition with the elevated potential from 1.65 to 1.8 V, which is corroded with a steep velocity to up to 2.17 V at 2.2 h [20,53]. This result reflects that the r-$TiO_2$ can effectively inhibit the oxidation of Ru to high valence state and improve the stability of $RuO_2$. On the other aspect, the TEM image (Figure S4) shows that the $RuO_2$@r-$TiO_2$ has no obvious shape change after the stability test, which confirms the function of the defective r-$TiO_2$ on the improvement of $RuO_2$ stability.

## 4 Conclusion

Synthesis and characterization of the $TiO_2$ support $RuO_2$ anode OER electrocatalyst were demonstrated in this work. $TiO_2$ with different structures endows the electrocatalysts with obviously different morphology and activity. The matching lattice ensures the strong interaction between $RuO_2$ and r-$TiO_2$, which adjusts the electronic structure of Ru and allows $RuO_2$ to directly grow on r-$TiO_2$ surface, leading to the formation of urchin-like structure with higher ECSA. Meanwhile, abundant oxygen vacancy of r-$TiO_2$ could suppress the oxidation of Ru to high valence state by providing/sharing electrons with Ru. Therefore, the $RuO_2$@r-$TiO_2$ exhibits remarkable OER activity, especially high TOF on active site and long-term stability compared with pure $RuO_2$ in an acidic aqueous solution. This study points out a path for further rational design and synthesis for high-efficiency precious metal of production.

*This work was supported by the National Key R&D Program of China (Grant No. 2020YFB1506802), the National Natural Science Foundation of China (Grant Nos. 21633008, U1601211, and 21733004), the Strategic Priority Research Program of the Chinese Academy of Sciences (Grant No. XDA21090400), and Jilin Province Science and Technology Development*

*Program (Grant Nos. 20190201300JC, 20170520150JH, and 20200201001JC).*

**Supporting Information**

The supporting information is available online at tech.scichina.com and link.springer.com. The supporting materials are published as submitted, without typesetting or editing. The responsibility for scientific accuracy and content remains entirely with the authors.


1 Stevens M B, Enman L J, Batchellor A S, et al. Measurement techniques for the study of thin film heterogeneous water oxidation electrocatalysts. Chem Mater, 2016, 29: 120–140
2 Zhang J, Zhang C, Sha J, et al. Efficient water-splitting electrodes based on laser-induced graphene. ACS Appl Mater Interfaces, 2017, 9: 26840–26847
3 Wu L K, Liu X Y, Hu J M. Electrodeposited $SiO_2$ film: A promising interlayer of a highly active Ti electrode for the oxygen evolution reaction. J Mater Chem A, 2016, 4: 11949–11956
4 Vignolo-González H A, Laha S, Jiménez-Solano A, et al. Toward standardized photocatalytic oxygen evolution rates using $RuO_2$@$TiO_2$ as a benchmark. Matter, 2020, 3: 464–486
5 Ri J H, Wu S, Jin J, et al. Growth of a sea urchin-like rutile $TiO_2$ hierarchical microsphere film on Ti foil for a quasi-solid-state dye-sensitized solar cell. Nanoscale, 2017, 9: 18498–18506
6 Thomas A G, Syres K L. Adsorption of organic molecules on rutile $TiO_2$ and anatase $TiO_2$ single crystal surfaces. Chem Soc Rev, 2012, 41: 4207
7 Lin J, Heo Y U, Nattestad A, et al. 3D hierarchical rutile $TiO_2$ and metal-free organic sensitizer producing dye-sensitized solar cells 8.6% conversion efficiency. Sci Rep, 2014, 4: 5769
8 Xiao M, Feng L, Zhu J, et al. Rapid synthesis of a PtRu nano-sponge with different surface compositions and performance evaluation for methanol electrooxidation. Nanoscale, 2015, 7: 9467–9471
9 Luo E, Xiao M, Ge J, et al. Selectively doping pyridinic and pyrrolic nitrogen into a 3D porous carbon matrix through template-induced edge engineering: Enhanced catalytic activity towards the oxygen reduction reaction. J Mater Chem A, 2017, 5: 21709–21714
10 Zhao X, Zhu J, Liang L, et al. Biomass-derived N-doped carbon and its application in electrocatalysis. Appl Catal B-Environ, 2014, 154-155: 177–182
11 Yang J, Wang B, Liu Y, et al. Enhancement of photovoltaic performance of photoelectrochemical biofuel cells by β-functionalized porphyrin sensitizers. J Power Sources, 2014, 248: 660–667
12 Xiao M, Li S, Zhu J, et al. Highly active PtAu nanowire networks for formic acid oxidation. Chem Plus Chem, 2014, 79: 1123–1128
13 Li G, Li S, Xiao M, et al. Nanoporous $IrO_2$ catalyst with enhanced activity and durability for water oxidation owing to its micro/mesoporous structure. Nanoscale, 2017, 9: 9291–9298
14 Audichon T, Napporn T W, Canaff C, et al. $IrO_2$ coated on $RuO_2$ as efficient and stable electroactive nanocatalysts for electrochemical water splitting. J Phys Chem C, 2016, 120: 2562–2573
15 Ma Z, Zhang Y, Liu S, et al. Reaction mechanism for oxygen evolution on $RuO_2$, $IrO_2$, and $RuO_2$@$IrO_2$ core-shell nanocatalysts. J Electroanal Chem, 2018, 819: 296–305
16 Wang Z, Xiao B, Lin Z, et al. *In-situ* surface decoration of $RuO_2$ nanoparticles by laser ablation for improved oxygen evolution reaction activity in both acid and alkali solutions. J Energy Chem, 2021, 54: 510–518
17 Trotochaud L, Ranney J K, Williams K N, et al. Solution-cast metal oxide thin film electrocatalysts for oxygen evolution. J Am Chem Soc, 2012, 134: 17253–17261
18 Song F, Hu X. Ultrathin cobalt-manganese layered double hydroxide is an efficient oxygen evolution catalyst. J Am Chem Soc, 2014, 136: 16481–16484
19 Tahir M, Pan L, Idrees F, et al. Electrocatalytic oxygen evolution reaction for energy conversion and storage: A comprehensive review. Nano Energy, 2017, 37: 136–157
20 Su J, Ge R, Jiang K, et al. Assembling ultrasmall copper-doped ruthenium oxide nanocrystals into hollow porous polyhedra: Highly robust electrocatalysts for oxygen evolution in acidic media. Adv Mater, 2018, 30: 1801351
21 Hao Z, Chen Q, Dai W, et al. Oxygen-deficient blue $TiO_2$ for ultrastable and fast lithium storage. Adv Energy Mater, 2020, 10: 1903107
22 Xu J, Dong W, Song C, et al. Black rutile (Sn, Ti)$O_2$ initializing electrochemically reversible Sn nanodots embedded in amorphous lithiated titania matrix for efficient lithium storage. J Mater Chem A, 2016, 4: 15698–15704
23 Zhou Y, Xie Z, Jiang J, et al. Lattice-confined Ru clusters with high CO tolerance and activity for the hydrogen oxidation reaction. Nat Catal, 2020, 3: 454–462
24 Saied S O, Sullivan J L, Choudhury T, et al. A comparison of ion and fast atom beam reduction in $TiO_2$. Vacuum, 1988, 38: 917–922
25 Stephan A M, Prem Kumar T, Thomas S, et al. $Ca_3(PO_4)_2$-incorporated poly(ethylene oxide)-based nanocomposite electrolytes for lithium batteries. Part II. Interfacial properties investigated by XPS and a.c. impedance studies. J Appl Polym Sci, 2012, 124: 3255–3263
26 Xiao Z, Huang Y C, Dong C L, et al. *Operando* identification of the dynamic behavior of oxygen vacancy-rich $Co_3O_4$ for oxygen evolution reaction. J Am Chem Soc, 2020, 142: 12087–12095
27 Rossmeisl J, Qu Z W, Zhu H, et al. Electrolysis of water on oxide surfaces. J Electroanal Chem, 2007, 607: 83–89
28 García-Mota M, Vojvodic A, Metiu H, et al. Tailoring the activity for oxygen evolution electrocatalysis on rutile $TiO_2$(110) by transition-metal substitution. ChemCatChem, 2011, 3: 1607–1611
29 Li G, Li S, Ge J, et al. Discontinuously covered $IrO_2$-$RuO_2$@Ru electrocatalysts for the oxygen evolution reaction: How high activity and long-term durability can be simultaneously realized in the synergistic and hybrid nano-structure. J Mater Chem A, 2017, 5: 17221–17229
30 Oh A, Kim H Y, Baik H, et al. Topotactic transformations in an icosahedral nanocrystal to form efficient water-splitting catalysts. Adv Mater, 2019, 31: 1805546
31 Wang Q, Xu C Q, Liu W, et al. Coordination engineering of iridium nanocluster bifunctional electrocatalyst for highly efficient and pH-universal overall water splitting. Nat Commun, 2020, 11: 4246
32 Jiang P, Chen J, Wang C, et al. Tuning the activity of carbon for electrocatalytic hydrogen evolution via an iridium-cobalt alloy core encapsulated in nitrogen-doped carbon cages. Adv Mater, 2018, 30: 1705324
33 Ma R, Zhou Y, Chen Y, et al. Ultrafine molybdenum carbide nanoparticles composited with carbon as a highly active hydrogen-evolution electrocatalyst. Angew Chem Int Ed, 2015, 54: 14723–14727
34 Zhang B, Zheng X, Voznyy O, et al. Homogeneously dispersed multimetal oxygen-evolving catalysts. Science, 2016, 352: 333–337
35 Feng J, Lv F, Zhang W, et al. Iridium-based multimetallic porous hollow nanocrystals for efficient overall-water-splitting catalysis. Adv Mater, 2017, 29: 1703798
36 Fan Z, Jiang J, Ai L, et al. Rational design of ruthenium and cobalt-based composites with rich metal-insulator interfaces for efficient and stable overall water splitting in acidic electrolyte. ACS Appl Mater Interfaces, 2019, 11: 47894–47903
37 DeSario P A, Chervin C N, Nelson E S, et al. Competitive oxygen evolution in acid electrolyte catalyzed at technologically relevant electrodes painted with nanoscale $RuO_2$. ACS Appl Mater Interfaces, 2017, 9: 2387–2395
38 Shan J, Guo C, Zhu Y, et al. Charge-redistribution-enhanced nanocrystalline Ru@$IrO_x$ electrocatalysts for oxygen evolution in acidic media. Chem, 2019, 5: 445–459
39 Feng Q, Wang Q, Zhang Z, et al. Highly active and stable ruthenate pyrochlore for enhanced oxygen evolution reaction in acidic medium electrolysis. Appl Catal B-Environ, 2019, 244: 494–501
40 Hu Y, Luo X, Wu G, et al. Engineering the atomic layer of $RuO_2$ on PdO nanosheets boosts oxygen evolution catalysis. ACS Appl Mater

Interfaces, 2019, 11: 42298–42304
41 Lee S W, Baik C, Pak C. Ordered mesoporous ruthenium oxide with balanced catalytic activity and stability toward oxygen evolution reaction. Catal Today, 2020, 358: 203–209
42 Kwon T, Yang H, Jun M, et al. Interfacing $RuO_2$ with Pt to induce efficient charge transfer from Pt to $RuO_2$ for highly efficient and stable oxygen evolution in acidic media. J Mater Chem A, 2021, 9: 14352–14362
43 Cui X, Ren P, Ma C, et al. Robust interface Ru centers for high-performance acidic oxygen evolution. Adv Mater, 2020, 32: 1908126
44 Xue Y, Fang J, Wang X, et al. Sulfate-functionalized $RuFeO_x$ as highly efficient oxygen evolution reaction electrocatalyst in acid. Adv Funct Mater, 2021, 31: 2101405
45 Chang C J, Chu Y C, Yan H Y, et al. Revealing the structural transformation of rutile $RuO_2$ via *in situ* X-ray absorption spectroscopy during the oxygen evolution reaction. Dalton Trans, 2019, 48: 7122–7129
46 Yao Y, Hu S, Chen W, et al. Engineering the electronic structure of single atom Ru sites via compressive strain boosts acidic water oxidation electrocatalysis. Nat Catal, 2019, 2: 304–313
47 Yi J, Lee W H, Choi C H, et al. Effect of Pt introduced on Ru-based electrocatalyst for oxygen evolution activity and stability. Electrochem Commun, 2019, 104: 106469
48 Zhao Z L, Wang Q, Huang X, et al. Boosting the oxygen evolution reaction using defect-rich ultra-thin ruthenium oxide nanosheets in acidic media. Energy Environ Sci, 2020, 13: 5143–5151
49 Lee S W, Baik C, Kim T Y, et al. Three-dimensional mesoporous Ir-Ru binary oxides with improved activity and stability for water electrolysis. Catal Today, 2020, 352: 39–46
50 Gao X, Chen J, Sun X, et al. Ru/$RuO_2$ nanoparticle composites with N-doped reduced graphene oxide as electrocatalysts for hydrogen and oxygen evolution. ACS Appl Nano Mater, 2020, 3: 12269–12277
51 Zhang L, Jang H, Liu H, et al. Sodium-decorated amorphous/crystalline $RuO_2$ with rich oxygen vacancies: A robust pH-universal oxygen evolution electrocatalyst. Angew Chem Int Ed, 2021, 60: 18821–18829
52 Wang K, Huang B, Zhang W, et al. Ultrathin RuRh@(RuRh)$O_2$ core@shell nanosheets as stable oxygen evolution electrocatalysts. J Mater Chem A, 2020, 8: 15746–15751
53 Kim J, Shih P C, Tsao K C, et al. High-performance pyrochlore-type yttrium ruthenate electrocatalyst for oxygen evolution reaction in acidic media. J Am Chem Soc, 2017, 139: 12076–12083
54 Bhowmik T, Kundu M K, Barman S. Growth of one-dimensional $RuO_2$ nanowires on g-carbon nitride: An active and stable bifunctional electrocatalyst for hydrogen and oxygen evolution reactions at all pH values. ACS Appl Mater Interfaces, 2016, 8: 28678–28688
55 Peng X, Zhao S, Mi Y, et al. Trifunctional single-atomic Ru sites enable efficient overall water splitting and oxygen reduction in acidic media. Small, 2020, 16: 2002888
56 Xu J, Lian Z, Wei B, et al. Strong electronic coupling between ultrafine iridium-ruthenium nanoclusters and conductive, acid-stable tellurium nanoparticle support for efficient and durable oxygen evolution in acidic and neutral media. ACS Catal, 2020, 10: 3571–3579
57 Cao L, Luo Q, Chen J, et al. Dynamic oxygen adsorption on single-atomic Ruthenium catalyst with high performance for acidic oxygen evolution reaction. Nat Commun, 2019, 10: 4849
58 Shan J, Ling T, Davey K, et al. Transition-metal-doped RuIr bifunctional nanocrystals for overall water splitting in acidic environments. Adv Mater, 2019, 31: 1900510